Supporting Information

Ground-State Structure of the Proton-Bound Formate Dimer by Cold-Ion Infrared Action Spectroscopy

Daniel A. Thomas,[a] Mateusz Marianski,[a] Eike Mucha,[a] Gerard Meijer,[a] Mark A. Johnson,*[b] and Gert von Helden*[a]

[a] Dr. D. A. Thomas, Dr. M. Marianski, E. Mucha, Prof. Dr. G. Meijer, Prof. Dr. G. von Helden
Fritz-Haber-Institut der Max-Planck-Gesellschaft
Faradayweg 4–6, 14195 Berlin (Germany)
E-mail: helden@fhi-berlin.mpg.de

[b] Prof. Dr. M. A. Johnson
Sterling Chemistry Laboratory
Yale University
225 Prospect Street, New Haven, CT 06520 (USA)
E-mail: mark.johnson@yale.edu

Table of Contents

Experimental Procedures

Infrared Action Spectroscopy of Ions Trapped in Helium Nanodroplets

The instrumentation utilized to obtain the infrared spectrum of ions trapped in helium nanodroplets has been described in several preceding publications.[1] Concisely, the instrument comprises a modified commercial quadrupole time-of-flight mass spectrometer coupled to custom chambers for helium nanodroplet formation, ion pickup, and spectroscopic interrogation. Ions are transferred to the gas phase by nanoelectrospray ionization (nESI), *m*/*z*-selected by a quadrupole mass filter, and directed *via* a DC bender into a hexapole ion trap. A fraction of these ions are then picked up by a pulsed beam of helium nanodroplets traversing the trap (average size of ~2 × 10^4 He atoms).[2] The helium droplets with embedded ions possess sufficient kinetic energy to escape the potential well of the hexapole trap and travel to the laser interaction region, where the helium nanodroplet beam overlaps with focused infrared radiation produced by the Fritz Haber Institute free-electron laser (FHI FEL).[3]

Resonant photon absorption by the embedded ions leads to evaporation of helium, and the sequential absorption of multiple photons yields free ions that can be detected by time-of-flight mass spectrometry.[1a, 1b, 4] The measurement of ion signal as a function of photon energy therefore provides an infrared spectrum of the embedded ions.[1d] Each data point represents an average of 25 repetitions of the ion ejection and detection process. As a first-order correction to the nonlinear dependence of ion signal intensity on transition strength and photon flux,[1a, 1b, 2, 4a] signal intensities are divided by the measured energy of the FEL macropulse. Additionally, regions of the spectrum where low-intensity features were observed were often measured with a higher photon flux (i.e., a more focused laser beam) to improve the signal intensity. The spectral region was then scaled to match the intensity measured at lower photon flux.

The formate dimer ions were generated by nESI of a 0.5% (v/v) aqueous solution of formic acid, formic acid-^{13}C, or formic acid-d_2 (Sigma-Aldrich, Munich, Germany). For measurement of the fully deuterated formate dimer, $[2DCOO^- + D^+]^-$, a 0.5/49.5/49.5% (v/v) solution of formic acid-d_2/CH_3OD/D_2O was utilized. In addition, a flow of nitrogen bubbled through a solution of D_2O was introduced as a cone gas at the atmospheric pressure inlet to reduce back-exchange of the shared deuteron for a proton during the transfer across the intermediate vacuum stages of the instrument.

Vibrational Predissociation Spectroscopy

Gas phase Ar-tagged formic acid anions were generated by passing 40 PSI Ar over a temperature-controlled (4.0-6.0°C) reservoir containing 90% formic acid; this mixture was expanded through a pulsed valve (General Valve, 0.5 mm orifice). The deuterated formic acid analogues were obtained using formic acid-d_2 (Sigma-Aldrich, 98 atom % D). The expansion was ionized using a counter-propagating 1 keV electron beam, and the ions of interest were mass-selected in the Yale double focusing, tandem time-of-flight (TOF) photofragmentation spectrometer described in detail previously.[17,20] The spectra reported here are averages of ~15 individual scans and include corrections for fluctuations in laser pulse energy over the scan range. The effective resolution of the spectrometer is ~4 cm^{-1} (FWHM) due to laser bandwidth and scan reproducibility.

Theoretical Chemical Calculations

Theoretical investigation of possible structures of the formate dimer was undertaken with calculations performed in Gaussian09 rev. D.01.[5] Relaxed dihedral angle scans and subsequent calculation of the harmonic vibrational modes of local minima were performed at the MP2/aug-cc-pVTZ level of theory.[6] Additionally, the accurate energies of local minima were computed from a complete basis set extrapolation scheme by Halkier et. al[7] using the aug-cc-pVnZ (n=3,4,5) basis sets and corrected for the difference between CCSD(T) and MP2 electron correlation energy using the aug-cc-pVTZ basis set.[8] Zero-point energy (ZPE) corrections were evaluated utilizing the harmonic approximation. For the fully symmetric structure **3**, ZPE corrections were taken from the fully symmetric geometry, although this geometry in fact corresponds to a transition state with an extremely low barrier height of less than 4×10^{-3} kJ/mol. Optimization and harmonic frequency calculations for local minima

were also performed at the MP2/ def2-TZVPP level of theory,[9] where structure **3** does not correspond to a transition state.

The reduced masses and cartesian displacement vectors for structure **1** obtained from harmonic frequency calculations at the MP2/aug-cc-pVTZ level of theory were further utilized to generate potential energy surfaces in a normal coordinate basis. Following the method of Tan and Kuo,[10] single point calculations at the MP2/aug-cc-pVTZ level of theory were utilized to generate a grid in each dimension (i.e., along each normal coordinate). In one dimension, the geometry at any point on the grid can be represented as

$$\xi_i(x,y,z) = \xi_{eq}(x,y,z) + n_i\Delta_i X_i(x,y,z)$$

where ξ_{eq} is the equilibrium geometry of the molecule, X_i is the cartesian displacement vector for normal mode i obtained from the Gaussian 09 output, Δ_i is the grid step size of normal mode i, and n_i is the step number, which adopts integer values from $-(n_{total}-1)/2$ to $(n_{total}-1)/2$, where n_{total} is the number of grid points. For 1D and 2D PES construction, 17 grid points were used, and 9 grid points were used for 4D PES construction. For a hypothetical three-dimensional grid consisting of normal modes i, j, and k, the geometry at any point on the grid is given by

$$\xi_{i,j,k}(x,y,z) = \xi_{eq}(x,y,z) + n_i\Delta_i X_i(x,y,z) + n_j\Delta_j X_j(x,y,z) + n_k\Delta_k X_k(x,y,z)$$

The relative step sizes for each normal mode fulfill the condition

$$\mu_i\Delta_i^2 = \mu_j\Delta_j^2 = \mu_k\Delta_k^2$$

where μ_i is the reduced mass of normal mode i.

To obtain the eigenstates and eigenvectors of the Hamiltonian for these potential energy surfaces, a discrete variable representation[11] was utilized, as previously described by Colbert and Miller.[12] The Hamiltonian matrix was constructed and diagonalized within Mathematica 11.1 (Wolfram, Oxfordshire, United Kingdom). A similar process was repeated to obtain the potential energy surfaces as well as eigenstates and eigenvectors of the vibrational Hamiltonian for the fully deuterated formate dimer.

To quantify the normal mode contributions to the coupled vibrational modes, eigenvectors obtained from multidimensional potential energy surfaces were decomposed as a linear combination of the outer products of eigenvectors in each component dimension (i.e., the outer product of eigenvectors from one-dimensional potentials). A least squares method was utilized to find the weighting factors in the linear combination. When the multidimensional and one-dimensional eigenvectors are first normalized, the relative contribution of each normal mode state is obtained as the square of the weighting coefficient in the linear combination. To obtain the atomic motion associated with the coupled vibrational modes from the two-dimensional potential, the squared coefficients were utilized as weighting factors for the Cartesian displacement vectors obtained from frequency calculations in Gaussian 09.

To calculate the intensity of transitions, dipole moment surfaces in a normal coordinate basis were also constructed. Specifically, the dipole moment component along the x, y, and z axes in Cartesian coordinates was obtained at each grid point as outlined above utilizing single-point energy calculations with the Gaussian command *nosymm*. Utilizing these surfaces and the eigenvectors obtained from DVR analysis of the PES, the transition dipole moment was calculated according to the formula

$$\langle \mu_x \rangle = \langle \psi_f(Q_1, Q_2, \dots, Q_n) | \mu_x(Q_1, Q_2, \dots, Q_n) | \psi_i(Q_1, Q_2, \dots, Q_n) \rangle$$

where ψ_f and ψ_i are the normalized wave functions of final state *f* and initial state *i*, and μ_x is the dipole moment along the Cartesian *x* axis. Practically, this value was calculated by finding the value of $\psi_f \mu_x \psi_i$ at each grid point and then integrating over all coordinate space utilizing an interpolating function. With the transition dipole moment in coulomb-meters, the intensity in km/mol of the transition $I_{f,i}$ between final state *f* and initial state *i* was then obtained according to the equation

$$I_{f,i} = \frac{1}{1000}\left(\frac{2\pi^2 N_A}{3c^2 \varepsilon_0 h^2}\right) E_{f,i} \left[(|\langle \mu_x \rangle|^2)^2 + \left(\left| \langle \mu_y \rangle \right|^2 \right)^2 + (|\langle \mu_z \rangle|^2)^2 \right]^{1/2}$$

where N_A is Avogadro's constant, c is the speed of light, $\hbar$ is the reduced Planck's constant, ε_0 is the permittivity of vacuum, and $E_{f,i}$ is the energy difference between *f* and *i* in joules.

Additional Experimental and Theoretical Infrared Spectra

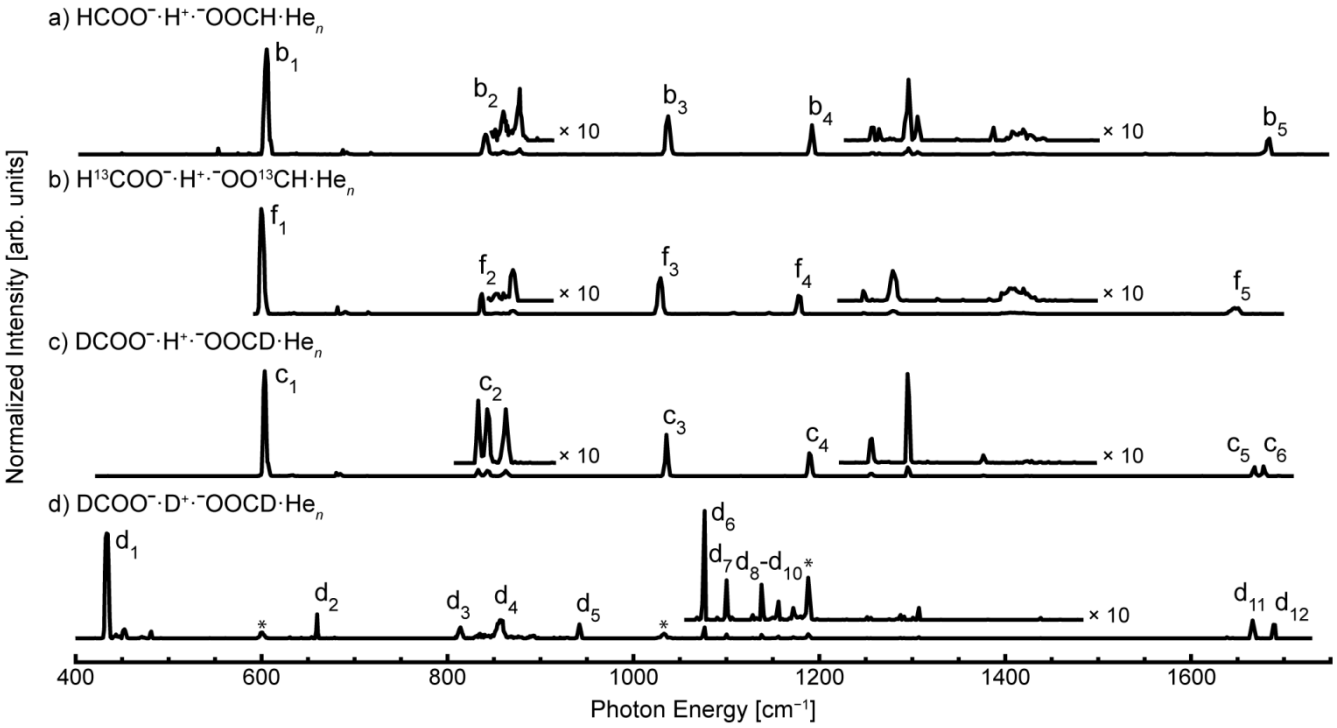

Figure S1. Vibrational spectra of the proton-bound dimer of formate and its isotopologues trapped in helium nanodroplets; the unlabeled dimer (a) exhibits a prominent transition at 605 cm^{-1}, with other strong features occurring at 841, 1037, 1192, and 1684 cm^{-1}. Only minor shifts in most features are observed upon ^{13}C substitution (b) or partial deuteration (c), whereas deuteration of the shared proton (d) results in a demonstrable shift of the most intense transition to 433 cm^{-1}. Features labeled with * in d result from proton back-exchange during ion trapping.

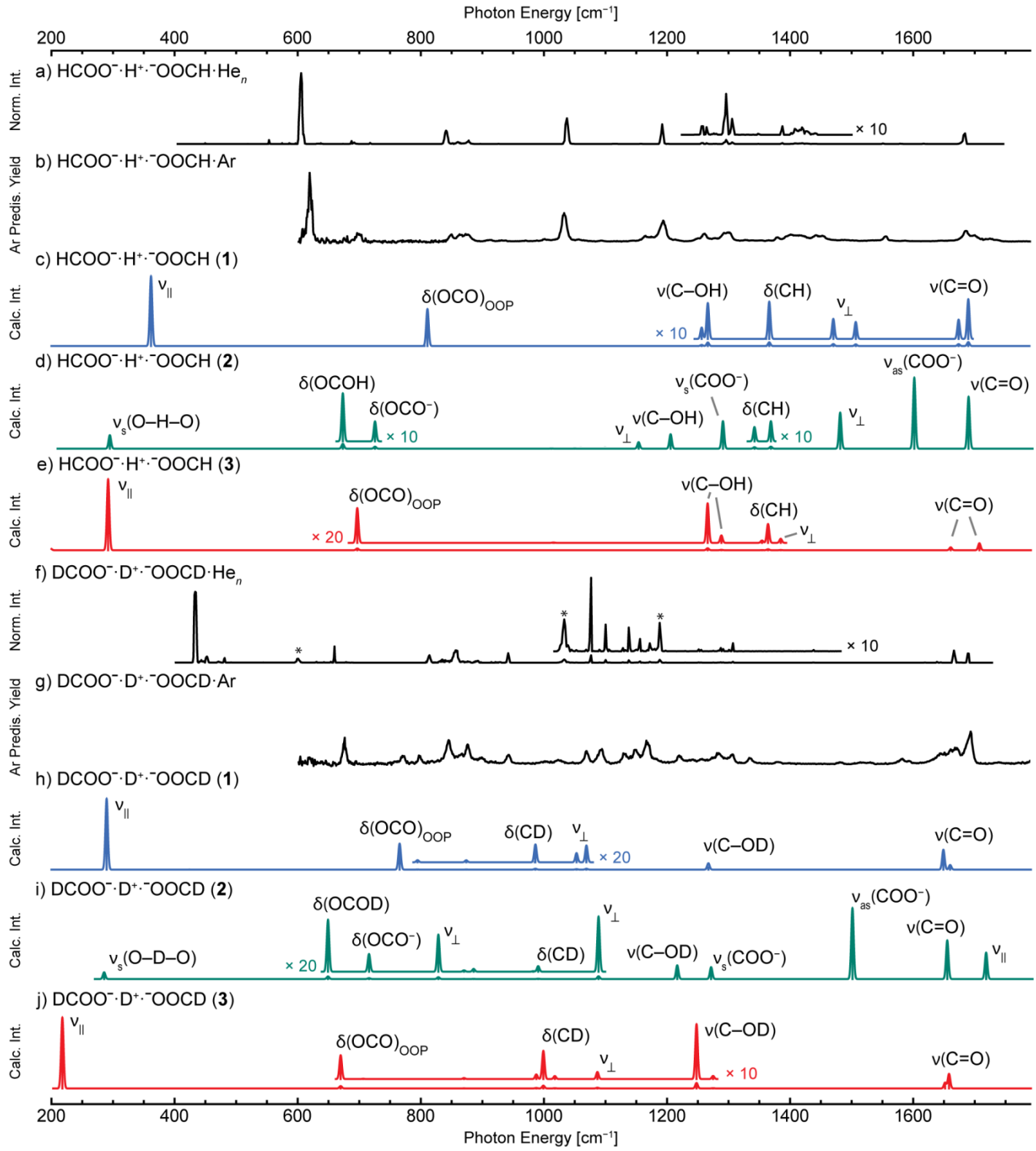

Figure S2. Comparison of experimental spectra for AHA⁻ (a, b) and ADA⁻ (f, g) to harmonic theoretical spectra (0.952 scaling factor) for low-energy structures **1** (c, h), **2** (d, i), and **3** (e, j). Structures **1** (blue) and **3** (red) feature a fully shared proton or deuteron, whereas structure **2** (green) exhibits a localized proton or deuteron and double contact structure (see Figure 2). Calculations were performed at the MP2/def2-TZVPP level of theory.

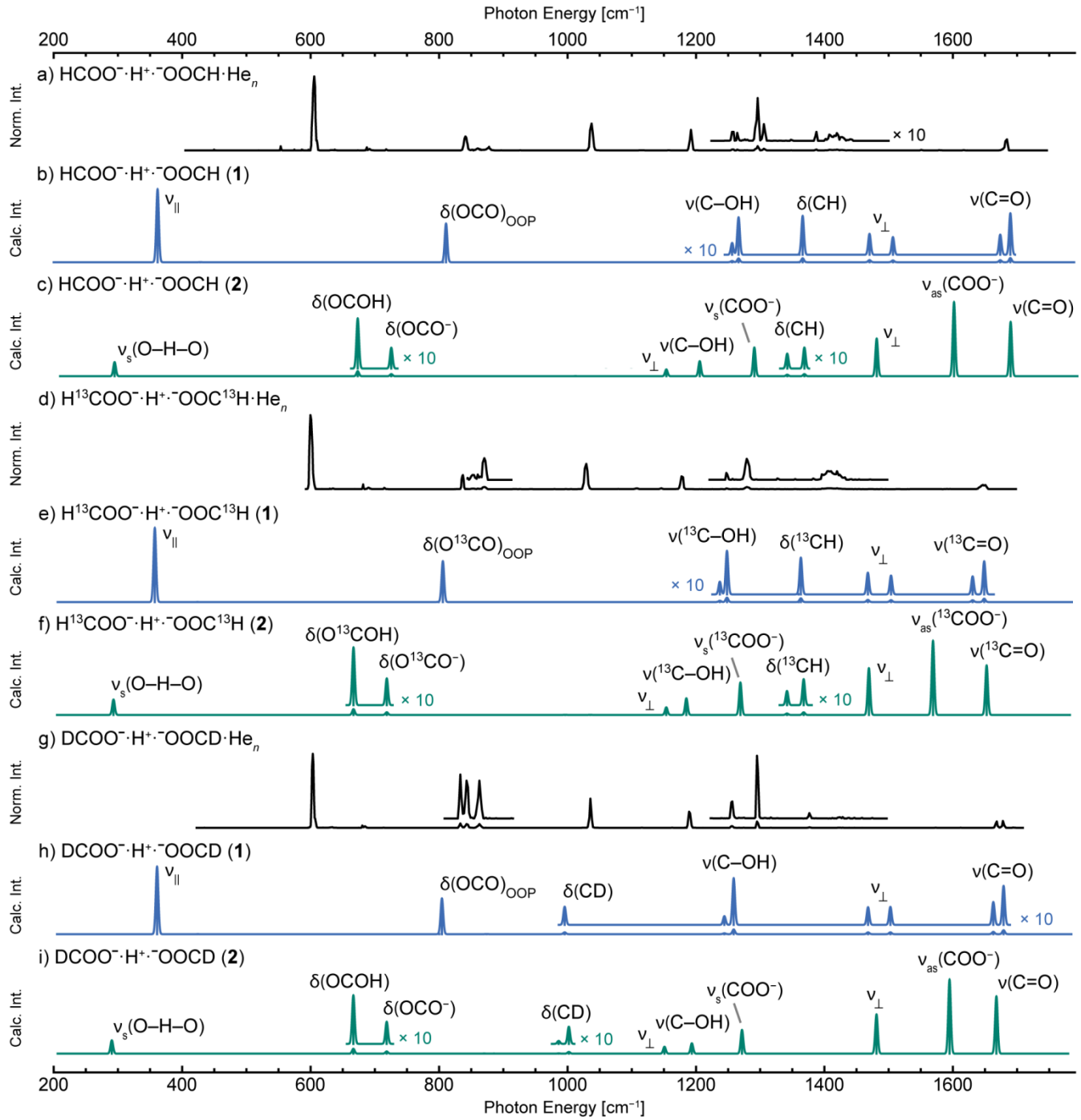

Figure S3. Comparison of experimental spectra for $HCOO^{-}\cdot H^{+}\cdot{}^{-}OOCH$ (a), $H^{13}COO^{-}\cdot H^{+}\cdot{}^{-}OOC^{13}H$ (d), and $DCOO^{-}\cdot H^{+}\cdot{}^{-}OOCD$ (g) to harmonic theoretical spectra (0.952 scaling factor) for low-energy structures **1** (b, e, h) and **2** (c, f, i). Structure **1** (blue) features a fully shared proton, whereas structure 2 (green) exhibits a localized proton and double contact structure (see Figure 2). Calculations were performed at the MP2/def2-TZVPP level of theory.

Tabulation of Experimental Spectral Line Positions

Table S1. Tabulation of Selected Spectra Lines for the Formate Proton-Bound Dimer and Isotopically Substituted Variants.[a]

Species	Band	Freq. [cm^{-1}]	Band	Freq. [cm^{-1}]	Band	Freq. [cm^{-1}]	Band	Freq. [cm^{-1}]	Band	Freq. [cm^{-1}]	Band	Freq. [cm^{-1}]	Band	Freq. [cm^{-1}]
HCOO$^-$·H$^+$·$^-$OOCH	**a$_1$**	619	**a$_2$**	849, 864, 875	**a$_3$**	1034	**a$_4$**	1194	**a$_5$**	1685, 1700				
HCOO$^-$·H$^+$·$^-$OOCH	**b$_1$**	605	**b$_2$**	841, 860, 878	**b$_3$**	1037	**b$_4$**	1192	**b$_5$**	1684				
H^{13}COO$^-$·H$^+$·$^-$OO^{13}CH	**f$_1$**	600	**f$_2$**	837, 870	**f$_3$**	1029	**f$_4$**	1178	**f$_5$**	1647				
DCOO$^-$·H$^+$·$^-$OOCD	**c$_1$**	603	**c$_2$**	833, 843, 862	**c$_3$**	1036	**c$_4$**	1190	**c$_5$**, **c$_6$**	1668, 1678				
DCOO$^-$·D$^+$·$^-$OOCD	**d$_1$**	433	**d$_2$**	660	**d$_3$**, **d$_4$**	814, 857	**d$_5$**	942	**d$_6$**, **d$_7$**	1077, 1100	**d$_8$**, **d$_9$**, **d$_{10}$**	1138, 1156, 1172	**d$_{11}$**, **d$_{12}$**	1666, 1689
DCOO$^-$·D$^+$·$^-$OOCD			**e$_1$**	676	**e$_2$**, **e$_3$**	845, 876	**e$_4$**	942	**e$_5$**, **e$_6$**	1069, 1092	**e$_7$**, **e$_8$**, **e$_9$**	1130, 1148, 1167	**e$_{10}$**, **e$_{11}$**	1667, 1693

[a] Band labels correspond to those given in Figure 2 and Figure S1.

Two-Dimensional PESs, Displacement Vectors, and Calculated Frequencies and Intensities

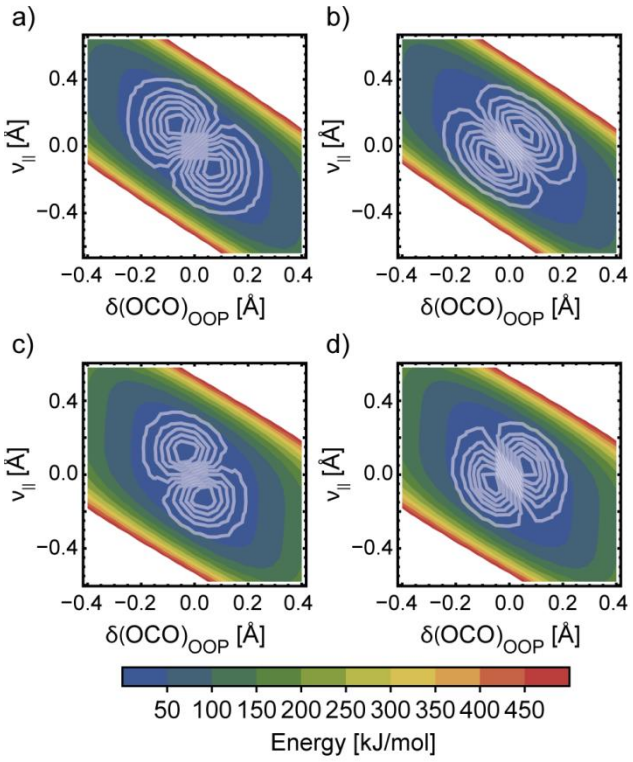

Figure S4. Two-dimensional potential energy surfaces and excited state eigenvectors of the vibrational Hamiltonian for AHA^- and ADA^-. The relative energy as a function of the Cartesian displacement vectors corresponding to the normal modes $\nu_{||}$ and $\delta(OCO)_{OOP}$ is shown in color for AHA^- (a, b) and ADA^- (c, d). The white contours superimposed on these potentials represent the eigenvectors of the first (a, c) and second (b, d) excited states of the vibrational Hamiltonian calculated utilizing the discrete variable representation (DVR) method.

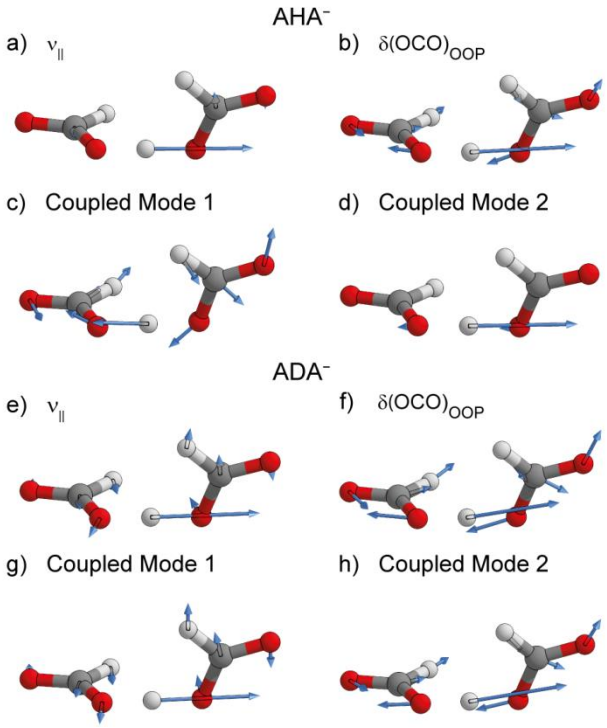

Figure S5. Displacement vectors of normal modes and coupled modes derived from 2D PES for AHA^- (a-d) and ADA^- (e-h). The harmonic normal modes for proton motion parallel to the shared proton axis, $\nu_{||}$ (a, e), and out-of-phase deformation of the two carboxylate moieties, $\delta(OCO)_{OOP}$ (b, f), exhibit large-amplitude displacement of the shared proton or deuteron. For AHA^-, a 2D PES reveals strong coupling of the modes (c, d), whereas the 2D PES for ADA^- indicates only weak coupling (g, h).

Table S2. Theoretical Frequencies and Intensities for AHA^- and ADA^- Derived from 1D and 2D PESs.[a]

Species	$\delta(OCO)_{OOP}$ 1D Freq. [cm^{-1}]	$\delta(OCO)_{OOP}$ 1D Int. [km mol^{-1}]	ν_{11} 1D Freq. [cm^{-1}]	ν_{11} 1D Int. [km mol^{-1}]	Coupled Mode 1 Freq. [cm^{-1}]	Coupled Mode 1 Int. [km mol^{-1}]	Coupled Mode 2 Freq. [cm^{-1}]	Coupled Mode 2 Int. [km mol^{-1}]
$HCOO^-{\cdot}H^+{\cdot}{}^-OOCH$	899.5	1896	899.0	3540	656.8	256	1213.5	5480
$DCOO^-{\cdot}D^+{\cdot}{}^-OOCD$	803.5	838	587.1	1933	544.2	885	891.1	2307

[a] One-dimensional frequencies (Freq.) and intensities (Int.) were calculated utilizing a discrete variable representation (DVR) along the cartesian displacement vector corresponding to the designated normal mode. The coupled modes are calculated utilizing DVR with a two-dimensional PES comprising the cartesian displacement vectors of the two normal modes.

Normal Mode Contributions for Two-Dimensional PESs

Table S3. Contributions of Outer Products of (1D) Normal Mode Eigenvectors to 2D PES Eigenvectors.[a]

$\Psi(\delta(OCO)_{OOP}, \nu_{11})$	$HCOO^{-}\cdot H^{+}\cdot^{-}OOCH$ Coupled Mode 1	$HCOO^{-}\cdot H^{+}\cdot^{-}OOCH$ Coupled Mode 2	$DCOO^{-}\cdot D^{+}\cdot^{-}OOCD$ Coupled Mode 1	$DCOO^{-}\cdot D^{+}\cdot^{-}OOCD$ Coupled Mode 2
$\Psi(0, 1)$	42.3	51.6	15.1	82.6
$\Psi(1, 0)$	51.6	40.4	82.3	14.6
$\Psi(2, 1)$	1.5	3.9	0.1	1.7
$\Psi(1, 2)$	2.9	3.8	2.0	0.8

[a] Values given in percent; percent contribution obtained as the square of the linear combination weighting coefficient for each normal mode excited state.

Displacement Vectors of ν_s(O–H–O) and $\delta(OCO)_{IP}$

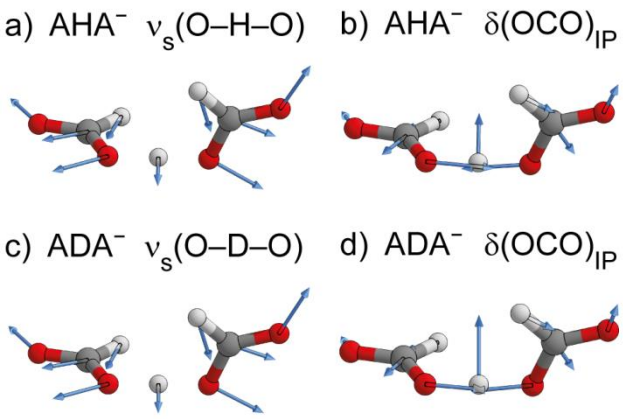

Figure S6. Additional displacement vectors for normal modes of AHA^- (a, b) and ADA^- (c, d). The normal modes for the O–H–O symmetric stretch, ν_s(O–H–O) (a, c), and in-phase carboxylate deformation, $\delta(OCO)_{IP}$ (b, d), strongly modulate the the interformate O–O distance.

Calculated Frequencies and Intensities from Four-Dimensional PESs

Table S4. Theoretical Frequencies and Intensities for AHA^- and ADA^- Derived from 4D PESs.[a]

Species	Freq. [cm^{-1}]	Int. [km mol^{-1}]	Freq. [cm^{-1}]	Int. [km mol^{-1}]	Freq. [cm^{-1}]	Int. [km mol^{-1}]	Freq. [cm^{-1}]	Int. [km mol^{-1}]
$HCOO^-{\cdot}H^{+}{\cdot}^-OOCH$	619	703	944	2055	1103	1295	1389	548
$DCOO^-{\cdot}D^{+}{\cdot}^-OOCD$	466	1181	786	490	918	716	-	-

[a] Only transitions with predicted frequency (Freq.) below 1400 cm^{-1} and predicted intensity (Int.) above 100 km mol^{-1} are tabulated.

Normal Mode Contributions for Four-Dimensional PESs

Table S5. Contributions of Outer Products of (1D) Normal Mode Eigenvectors to 4D PES Eigenvectors for $HCOO^{-}\cdot H^{+}\cdot {}^{-}OOCH$.[a]

$\Psi(\delta(OCO)_{IP}, \nu_s(O–H–O), \delta(OCO)_{OOP}, \nu_{\perp\perp})$	$\Psi_{618.5}$	$\Psi_{943.5}$	$\Psi_{1103.4}$	$\Psi_{1389.3}$
Ψ(0, 0, 0, 1)	53.3	1.1	20.6	6.7
Ψ(0, 0, 1, 0)	24.1	45.9	5.0	13.5
Ψ(0, 1, 0, 0)	0.0	0.0	0.0	0.0
Ψ(1, 0, 0, 0)	0.0	0.0	0.0	0.0
Ψ(0, 1, 0, 1)	9.3	25.5	13.0	0.5
Ψ(0, 1, 1, 0)	1.4	0.7	39.1	24.3
Ψ(1, 0, 0, 1)	2.5	2.7	2.8	0.1
Ψ(1, 0, 1, 0)	0.2	1.1	0.5	0.6
Ψ(0, 0, 2, 1)	0.5	1.9	0.2	1.2
Ψ(0, 0, 1, 2)	2.6	0.0	0.8	0.8
Ψ(0, 2, 0, 1)	1.0	9.0	4.6	21.6
Ψ(0, 2, 1, 0)	0.0	0.1	5.2	1.4
Ψ(0, 3, 0, 1)	0.1	1.3	0.5	9.6
Ψ(1, 1, 0, 1)	0.7	3.9	0.1	2.2
Ψ(1, 1, 1, 0)	0.0	0.2	1.0	0.5
Ψ(1, 2, 0, 1)	0.1	1.3	0.2	5.1

[a] Values given in percent; percent contribution obtained as the square of the linear combination weighting coefficient for each normal mode excited state. Vibrational eigenstates are denoted by their energy above the ground state.

Table S6. Contributions of Outer Products of (1D) Normal Mode Eigenvectors to 4D PES Eigenvectors for $DCOO^{-}\cdot D^{+}\cdot{}^{-}OOCD$.[a]

$\Psi(\delta(OCO)_{IP}, \nu_s(O–H–O), \delta(OCO)_{OOP}, \nu_{||})$	$\Psi_{465.8}$	$\Psi_{785.9}$	$\Psi_{918.2}$
Ψ(0, 0, 0, 1)	71.4	1.3	17.3
Ψ(0, 0, 1, 0)	4.0	62.0	22.4
Ψ(0, 1, 0, 0)	0.0	0.0	0.0
Ψ(1, 0, 0, 0)	0.0	0.0	0.0
Ψ(0, 1, 0, 1)	12.8	18.6	22.4
Ψ(0, 1, 1, 0)	0.0	1.9	9.9
Ψ(1, 0, 0, 1)	3.4	0.8	1.3
Ψ(1, 0, 1, 0)	0.0	0.7	0.5
Ψ(0, 0, 2, 1)	0.0	0.6	0.3
Ψ(0, 0, 1, 2)	1.2	0.1	0.3
Ψ(0, 2, 0, 1)	1.4	7.0	12.1
Ψ(0, 2, 1, 0)	0.0	0.2	0.3
Ψ(0, 3, 0, 1)	0.1	1.0	2.2
Ψ(1, 1, 0, 1)	0.9	2.0	1.3
Ψ(1, 1, 1, 0)	0.0	0.1	0.1
Ψ(1, 2, 0, 1)	0.2	0.7	1.0

[a] Values given in percent; percent contribution obtained as the square of the linear combination weighting coefficient for each normal mode excited state. Vibrational eigenstates are denoted by their energy above the ground state.

Parameters and Energies of Theoretical Structures

Table S7. Equilibrium Geometry of $HCOO^{-}{\cdot}H^{+}{\cdot}{}^{-}OOCH$ Structure **1**.[a]

Atom	x	y	z
O	0.12956	3.07807	-0.40487
C	-0.12956	1.89452	-0.19098
O	0.50963	1.09227	0.59908
H	-0.99065	1.42375	-0.70492
O	-0.50963	-1.09227	0.59908
C	0.12956	-1.89452	-0.19098
O	-0.12956	-3.07807	-0.40487
H	0.99065	-1.42375	-0.70492
H	-0.00000	-0.00000	0.59415

[a] Optimization at the MP2/aug-cc-pVTZ level of theory, with coordinates in Angstroms.

Table S8. Equilibrium Geometry of $HCOO^{-}{\cdot}H^{+}{\cdot}{}^{-}OOCH$ Structure **2**.[a]

Atom	x	y	z
O	2.74437	0.49863	0.00041
C	1.54833	0.23970	0.00030
O	1.06170	-0.98301	-0.00105
H	0.77180	1.01686	0.00135
O	-1.45379	-1.01539	0.00075
C	-2.09330	0.08863	0.00017
O	-1.64210	1.24826	-0.00061
H	-3.19860	-0.03327	0.00035
H	0.01506	-0.94145	-0.00044

[a] Optimization at the MP2/aug-cc-pVTZ level of theory, with coordinates in Angstroms.

Table S9. Equilibrium Geometry of $HCOO^{-}{\cdot}H^{+}{\cdot}{}^{-}OOCH$ Structure **3**.[a]

Atom	x	y	z
O	2.31083	0.71563	-0.55671
C	2.05644	-0.35270	0.00103
O	0.94307	-0.75569	0.51518
H	2.85647	-1.11230	0.10563
O	-2.31083	-0.71579	-0.55654
C	-2.05644	0.35271	0.00089
O	-0.94307	0.75584	0.51494
H	-2.85647	1.11234	0.10525
H	0.00003	0.00004	0.44255

[a] Optimization at the MP2/aug-cc-pVTZ level of theory, with coordinates in Angstroms.

Table S10. Calculated Energies of $HCOO^{-}\cdot H^{+}\cdot {}^{-}OOCH$ Structures **1**, **2**, and **3**.[a]

Structure Number	Energy MP2/ aug-cc-pVTZ	Zero-Point Energy MP2/ aug-cc-pvTZ	Energy MP2/ aug-cc-pVQZ	Energy MP2/ aug-cc-pV5Z	Energy CCSD(T)/ aug-cc-pVTZ	Energy CBS + CCSD(T) Correction
1	-378.468086	0.052217	-378.574982	-378.613778	-378.524282	-378.69207
2	-378.469150	0.055585	-378.576136	-378.615046	-378.526329	-378.69447
3	-378.46149	0.051295	-378.568456	-378.607298	-378.517726	-378.68568

[a] Optimization at the MP2/aug-cc-pVTZ level of theory, with single point energy calculations at higher levels of theory; all values reported in Hartrees.

References

[1] a) F. Filsinger, D.-S. Ahn, G. Meijer, G. von Helden, *Phys. Chem. Chem. Phys.* **2012**, *14*, 13370-13377; b) A. I. González Flórez, D.-S. Ahn, S. Gewinner, W. Schöllkopf, G. von Helden, *Phys. Chem. Chem. Phys.* **2015**, *17*, 21902-21911; c) A. I. González Flórez, E. Mucha, D.-S. Ahn, S. Gewinner, W. Schöllkopf, K. Pagel, G. von Helden, *Angew. Chem., Int. Ed.* **2016**, *55*, 3295–3299; d) E. Mucha, A. I. González Flórez, M. Marianski, D. A. Thomas, W. Hoffmann, W. B. Struwe, H. S. Hahm, S. Gewinner, W. Schöllkopf, P. H. Seeberger, G. von Helden, K. Pagel, *Angew. Chem., Int. Ed.* **2017**, *56*, 11248-11251.

[2] A. I. González Flórez, Dr. rer. nat. Thesis, Free University Berlin (Berlin), **2015**.

[3] W. Schöllkopf, S. Gewinner, H. Junkes, A. Paarmann, G. von Helden, H. Bluem, A. M. M. Todd, *Proc. SPIE* **2015**, *9512*, 95121L.

[4] a) S. Smolarek, N. B. Brauer, W. J. Buma, M. Drabbels, *J. Am. Chem. Soc.* **2010**, *132*, 14086-14091; b) X. Zhang, N. B. Brauer, G. Berden, A. M. Rijs, M. Drabbels, *J. Chem. Phys.* **2012**, *136*, 044305.

[5] Gaussian 09, Revision D.01, M. J. Frisch, G. W. Trucks, H. B. Schlegel, G. E. Scuseria, M. A. Robb, J. R. Cheeseman, G. Scalmani, V. Barone, G. A. Petersson, H. Nakatsuji, X. Li, M. Caricato, A. Marenich, J. Bloino, B. G. Janesko, R. Gomperts, B. Mennucci, H. P. Hratchian, J. V. Ortiz, A. F. Izmaylov, J. L. Sonnenberg, D. Williams-Young, F. Ding, F. Lipparini, F. Egidi, J. Goings, B. Peng, A. Petrone, T. Henderson, D. Ranasinghe, V. G. Zakrzewski, J. Gao, N. Rega, G. Zheng, W. Liang, M. Hada, M. Ehara, K. Toyota, R. Fukuda, J. Hasegawa, M. Ishida, T. Nakajima, Y. Honda, O. Kitao, H. Nakai, T. Vreven, K. Throssell, J. A. Montgomery, Jr., J. E. Peralta, F. Ogliaro, M. Bearpark, J. J. Heyd, E. Brothers, K. N. Kudin, V. N. Staroverov, T. Keith, R. Kobayashi, J. Normand, K. Raghavachari, A. Rendell, J. C. Burant, S. S. Iyengar, J. Tomasi, M. Cossi, J. M. Millam, M. Klene, C. Adamo, R. Cammi, J. W. Ochterski, R. L. Martin, K. Morokuma, O. Farkas, J. B. Foresman, and D. J. Fox, Gaussian, Inc., Wallingford CT, **2009**.

[6] a) R. A. Kendall, T. H. Dunning, Jr., R. J. Harrison, *J. Chem. Phys.* **1992**, *96*, 6796-6806; b) C. Møller, M. S. Plesset, *Phys. Rev.* **1934**, *46*, 618-622.

[7] A. Halkier, T. Helgaker, P. Jørgensen, W. Klopper, J. Olsen, *Chem. Phys. Lett.* **1999**, *302*, 437-446.

[8] M. O. Sinnokrot, E. F. Valeev, C. D. Sherrill, *J. Am. Chem. Soc.* **2002**, *124*, 10887-10893.

[9] a) F. Weigend, R. Ahlrichs, *Phys. Chem. Chem. Phys.* **2005**, *7*, 3297-3305; b) F. Weigend, *Phys. Chem. Chem. Phys.* **2006**, *8*, 1057-1065.

[10] J. A. Tan, J.-L. Kuo, *J. Phys. Chem. A* **2015**, *119*, 11320-11328.
[11] J. C. Light, T. Carrington, in *Advances in Chemical Physics*, John Wiley & Sons, Inc., **2007**, pp. 263-310.
[12] D. T. Colbert, W. H. Miller, *J. Chem. Phys.* **1992**, *96*, 1982-1991.

Author Contributions

G.M., M.A.J., and G.v.H oversaw and directed the research project.

E.M. and D.A.T. carried out helium nanodroplet experiments.

M.M. and D.A.T. performed *ab initio* calculations.

All authors contributed to data analysis and the writing of the manuscript.